Ultra-high vacuum scanning tunneling microscopy and theoretical studies of 1-halohexane monolayers on graphite

Thomas Müller*†, Tova L. Werblowsky†, Gina M. Florio, Bruce J. Berne, and George W. Flynn‡

Department of Chemistry and Columbia Materials Research Science and Engineering Center, Columbia University, New York, NY 10027

This contribution is part of the special series of Inaugural Articles by members of the National Academy of Sciences elected on May 1, 2001.

Contributed by George W. Flynn, December 27, 2004

A simple model system for the 2D self-assembly of functionalized organic molecules on surfaces was examined in a concerted experimental and theoretical effort. Monolayers of 1-halohexanes were formed through vapor deposition onto graphite surfaces in ultrahigh vacuum. Low-temperature scanning tunneling microscopy allowed the molecular conformation, orientation, and monolayer crystallographic parameters to be determined. Essentially identical noncommensurate monolayer structures were found for all 1-halohexanes, with differences in image contrast ascribed mainly to electronic factors. Energy minimizations and molecular dynamics simulations reproduced structural parameters of 1-bromohexane monolayers quantitatively. An analysis of interactions driving the self-assembly process revealed the crucial role played by small but anisotropic electrostatic forces associated with the halogen substituent. While alkyl chain dispersion interactions drive the formation of a close-packed adsorbate monolayer, electrostatic headgroup forces are found to compete successfully in the control of both the angle between lamella and backbone axes and the angle between surface and backbone planes. This competition is consistent with energetic tradeoffs apparent in adsorption energies measured in earlier temperature-programmed desorption studies. In accordance with the higher degree of disorder observed in scanning tunneling microscopy images of 1-fluorohexane, theoretical simulations show that electrostatic forces associated with the fluorine substituent are sufficiently strong to upset the delicate balance of interactions required for the formation of an ordered monolayer. The detailed dissection of the driving forces for self-assembly of these simple model systems is expected to aid in the understanding of the more complex self-assembly processes taking place in the presence of solvent.

haloalkanes | conformation | simulations

Future advances in nanoscale science and engineering are expected to rely increasingly on the controlled bottom-up assembly of molecular arrays. The successful creation of targeted molecular device structures demands a fundamental understanding of the interactions governing 2D self-organization. Simple functionalized hydrocarbon molecules are known to form self-ordered structures at a variety of surfaces and interfaces (1–32) and can serve as ideal model systems to study the underlying forces driving the self-assembly process.

Numerous experimental(1–10, 13, 14, 16–19, 21, 22, 24, 27, 28, 30–41) and theoretical (39, 42, 43) studies have investigated the self-assembled monolayers formed when a melt or solution containing alkanes or their derivatives is brought in contact with the basal plane of a graphite substrate. Scanning tunneling microscopy (STM) (2–6, 8–10, 13, 14, 16–19, 24, 27, 28, 31–38, 40, 41) and diffraction-based probes (7, 39, 44, 45) have been used to characterize the crystallographic monolayer parameters as well as the orientation and conformation of the constituent molecular species. For many alkane derivatives, STM images have revealed the formation of large, ordered adsorbate domains composed of parallel, close-packed molecules with their carbon skeleton in an extended all-trans conformation, oriented parallel to the surface plane. The Van der Waals forces associated with the saturated hydrocarbon chains provide intermolecular and molecule–surface interactions that play an important role in establishing the observed structures. However, many subtle modifications of the self-assembled structures have been observed, depending on alkane functionalization and chain length (3, 6, 10–12, 15, 17–19, 28, 35, 36, 41, 46). Specific headgroup interactions (e.g., hydrogen bonding and electrostatic forces) (11, 12, 17, 19, 28, 41) and geometric subtleties (e.g., odd vs. even chain length) (31, 32, 36) also can have a profound influence on the self-assembly. The resulting set of interactions creates competing constraints, which are evident in the calculated and measured adsorption energies (47).

The present study focuses on functionalized alkanes of modest chain length where both functional group and alkyl chain interactions are expected to be important. The self-assembly is examined in ultrahigh vacuum, thus providing the most direct connection with theoretical simulations without the need for solvent models. By dissecting the balance of interactions in this simple model system, the stage will be set for a better understanding of more complex systems assembling at the liquid/solid interface, where the presence of solvent leads to modified interaction forces (7, 10).

Experimental Procedures

All experiments were conducted in an ultrahigh vacuum (UHV) system with a base pressure of $\approx 2 \times 10^{-10}$ torr (1 torr = 133 Pa). The chamber was equipped with a quadrupole mass spectrometer (RGA 200, Stanford Research, Sunnyvale, CA) and a commercial variable temperature STM (Omicron Nanotechnology, Taunusstein, Germany) capable of scanning at temperatures ranging from 25 to 1,500 K. Monolayers of 1-fluorohexane, 1-chlorohexane, 1-bromohexane, and 1-iodohexane were formed by delivering the compound under investigation through a retractable line doser directly to the cooled highly oriented pyrolytic graphite (HOPG) substrate positioned inside the STM sample stage. A pinhole with 5-μm diameter controlled the molecular flux emerging from the line doser, resulting in typical doses of 1–10 liters for backing pressures of $\approx$2 torr and dosing times on the order of 30 s. Guided by the results from our previous temperature-programmed desorption studies (47), substrate temperatures during dosing were chosen to permit monolayer formation while ensuring rapid desorption

Abbreviations: HOPG, highly oriented pyrolytic graphite; LJ, Lennard–Jones; NVT, number/volume/temperature; OPLS, optimized potentials for liquid simulations; STM, scanning tunneling microscopy; UHV, ultrahigh vacuum.

See accompanying Biography on page 5312.

*Present address: Veeco Metrology Group, 112 Robin Hill Road, Santa Barbara, CA 93117.

†T.M. and T.L.W. contributed equally to this work.

‡To whom correspondence should be addressed. E-mail: flynn@chem.columbia.edu.

(i.e., on a timescale of seconds) of any excess molecules forming additional adsorption layers. In particular, 1-fluorohexane, 1-chlorohexane, 1-bromohexane, and 1-iodohexane were dosed at substrate temperatures of 150, 170, 180, and 190 K, respectively, with an estimated uncertainty of ±5 K. After dosing, the substrate temperature was lowered slowly (i.e., at a rate of <0.1 K/s) to 80 K for imaging. All images were obtained in the constant current mode and were subjected to a background correction. Based on a careful analysis of measured adsorbate structural parameters as a function of absolute scan speed, small-scale images were additionally corrected for constant drift in the image plane. The tunneling parameters are given in the legends of Figs. 1–6 and also Figs. 7–9, which are published as supporting information on the PNAS web site, with the sign of the voltage referred to the sample.

All 1-halohexanes were obtained from Aldrich and were degassed by at least 10 freeze–pump–thaw cycles before dosing. To ensure the presence in the gas phase of the compound under consideration (i.e., as opposed to more volatile impurities), mass spectra recorded before STM experiments were compared with published spectra (NIST Standard Reference Database Number 69, National Institute of Standards and Technology, 2003, www.nist.gov/srd/online.htm). Immediately before insertion into the UHV system via a turbo-pumped loadlock, the HOPG substrate (ZYB grade; Advanced Ceramics, Lakewood, OH) was cleaved in air to expose a fresh, atomically flat basal plane of graphite. Before each STM experiment, the HOPG substrate was heated *in situ* to ≈973 K to remove contaminants. STM tips were prepared by electrochemical etching of a polycrystalline tungsten wire and were annealed up to ≈973 K upon introduction into the UHV chamber.

Computational Methods

The SIM molecular dynamics program (H. A. Stern, H. Xu, E. Harder, F. Rittner, M. Pavese, and B.J.B., unpublished work) was used for all of the calculations described here. The united-atom optimized potentials for liquid simulations (OPLS) force field (48) was used for the intramolecular and intermolecular adsorbate interactions with a geometric combining rule for the calculation of parameters for unlike atoms (i.e., $\sigma_{as} = \sqrt{\sigma_{aa}\sigma_{ss}}$ and $\varepsilon_{as} = \sqrt{\varepsilon_{aa}\varepsilon_{ss}}$). The terms included in the potential energy expression for the adsorbate were:

$$E_{\text{stretch}} + E_{\text{bend}} + E_{\text{torsion}} + E_{\text{electrostatic}} + E_{\text{Lennard–Jones}}.$$

The bond energy is represented by a simple harmonic model, as is the bending angular energy. The torsion is modeled as a Fourier expansion in the dihedral angles, and the fitted parameters are the coefficients of this expansion. The electrostatic term calculates the energy between two point charges, which for this system are placed only on the halogen atom and the methylene group directly bound to it. The Lennard–Jones (LJ) energy uses a standard 6–12 potential to describe the Van der Waals interactions in terms of the relevant repulsive and dispersive contributions. The electrostatic and LJ parameters for the alkyl chains were taken from the standard united-atom OPLS parameter files, whereas the halogenated functionals were specially fitted in the BOSS simulation program (49) to extract more exact electrostatic and Van der Waals information for these atoms. Comparisons then were made to parameters derived from other semiclassical fits (CM3/AM1 and CM3/PM3) (50, 51). The results gave identical partial charges for the Br and F headgroups (−0.22 e) by using the BOSS method for united-atom OPLS parameter fitting.

To describe the interaction of the adsorbate with the graphite substrate, a static Steele potential (52) was used in combination with an image charge interaction term. The latter is commonly included (53) to describe the effect of placing a semimetallic surface in close proximity to a set of static external charges (54), in this case the partial point charges assigned to the molecular headgroups. The image charge interaction assigns an equal but opposite charge to an image of each point charge reflected through the image plane, which is located at $z_{\text{image}} = d/2$. The distance d in this system is the graphite interlayer spacing (3.35 Å), and the convention for the z coordinate system in these types of simulations places the topmost graphite layer sheet at the $z = 0$ position. Each molecular point charge interacts with its own image and all of the other images, but the image charges do not interact with each other in this model. A Steele potential, which describes the graphite surface by using a Fourier expansion in the graphite lattice vectors, was used for the substrate–adsorbate Van der Waals interaction. The top two layers are modeled as a full corrugated potential, and the rest of the substrate is included as a smooth attractive potential for a total of 40 layers of graphite. The parameters used for the Steele potential ($\sigma_{\text{surface}} = 3.55$ Å, $\varepsilon_{\text{surface}} = 0.07$ kcal), when used with a geometric combining rule and the standard OPLS alkyl parameters, were found to closely match the previously reported values (55, 56) used to compare calculated and experimental melting temperatures of alkane monolayers on graphite surfaces.

All of the minimizations were performed by using the Truncated Newton algorithm package TNPACK (57) within SIM. Molecular dynamics in SIM were carried out at constant number/volume/temperature (NVT), by using the Nose–Hoover chains method (58, 59) for the proper equilibration of the bath temperature in the canonical ensemble.

Results and Discussion

Overview of STM Images and the Spatial Structure of the Adsorbate Monolayers. The spatial structure within individual adsorbate domains of 1-fluorohexane, 1-chlorohexane, 1-bromohexane, and 1-iodohexane, respectively, can be seen in the medium-scale constant current STM topographs shown in Fig. 1. Guided by the results from past temperature-programmed desorption studies (47) and the desire to obtain "annealed" monolayers, substrate temperatures during vapor deposition of each adsorbate species were chosen to permit the formation of monolayers on graphite, while also providing maximum thermal energy and ensuring rapid desorption of the respective adsorbate species from multilayer sites. Subsequent slow cooling was expected to produce a thermodynamically controlled, monolayer adsorbate structure at high (i.e., close to monolayer) coverage.

In agreement with expectations, all STM images displayed in Fig. 1 show a contiguous adsorbate layer with a high degree of order. Ordered monolayers of alkyl derivatives on graphite surfaces generally exhibit a lamellar structure (3–6, 15, 17, 41), with individual molecules assuming the energetically favorable all-trans conformation (3–6, 15, 17, 41). The STM images shown in Fig. 1 support the formation of such a lamellar structure in the present case.

Fig. 2 shows high-resolution STM images of all 1-halohexane monolayers at submolecular resolution. Although the strong moiré effect in these images (see *STM Image Contrast: Electronic and Spatial Factors*) prevents the unambiguous assignment of bright spots to individual sections (e.g., CH_2 units) of the hydrocarbon backbone, the sufficiently distinct contrast of endgroups (i.e., CH_3 and the halogen substituent) permits the measurement of distances between adjacent lamellae as well as adjacent molecules within lamellae. Thus, adsorbate structures can be proposed as illustrated by the superimposed molecular arrays in Fig. 2 with structural parameters summarized in Table 1. All 1-halohexane monolayers are characterized by lamellar spacings (a) of ≈2 nm, neighbor distances (b) (measured along the lamella direction) of ≈0.5 nm, neighbor distances (c) (measured perpendicular to the molecular backbone) of ≈0.45 nm, and lamella–backbone angles (ϕ) of close to ≈60°. Aside from providing a satisfactory explanation of STM spot patterns, the proposed structures imply reasonable intermolecular distances in the context of monolayers and crystals formed by related species.

In general, monolayers of alkyl derivatives on graphite exhibit

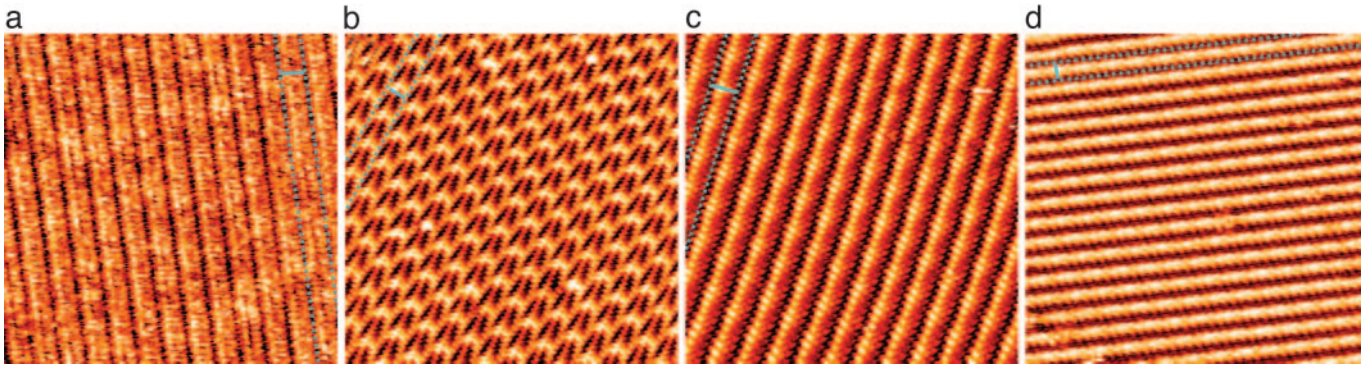

Fig. 1. Medium-size STM topographs of 1-halohexane monolayers on HOPG. The constant current STM topographs of 1-fluorohexane (25 × 25 nm, V_{bias} = 2.0 V, I_{setp} = 100 pA) (*a*), 1-chlorohexane (30 × 30 nm, V_{bias} = 2.0 V, I_{setp} = 90 pA) (*b*), 1-bromohexane (25 × 25 nm, V_{bias} = 2.0 V, I_{setp} = 100 pA) (*c*), and 1-iodohexane (25 × 25 nm, V_{bias} = 2.0 V, I_{setp} = 75 pA) (*d*) all were acquired at $T_{substrate}$ = 80 K. However, self-assembled monolayers were formed by vapor deposition at higher substrate temperatures, guided by results from previous desorption studies (47). In each image, the dotted blue lines indicate the lamella direction (*b*) and the spacing between them (marked by a blue bar) is equal to the length of two 1-halohexane molecules.

intermolecular distances ranging from ≈4.2 to ≈4.8 Å (4, 5), corresponding to the intermolecular distances in 3D alkane crystals measured perpendicular and parallel to the plane formed by the all-trans carbon backbone, respectively (60). In the present case, the neighbor distances (*c*) fall exactly into this range. The proposed structure, with the molecular plane formed by the carbon skeleton essentially parallel to the surface plane, would suggest neighbor distances (*c*) on the order of 4.8 Å. This value is in agreement (within uncertainty) with the experimental measurements, with the lack of commensurability as evidenced by the moiré pattern (see *STM Image Contrast: Electronic and Spatial Factors*) and with theoretical predictions (see *Results from Theoretical Stimulations: Driving Forces for Self-Assembly*). In this all-trans configuration, the carbon–halogen bond lies in the molecular plane formed by the carbon–carbon bonds, and the size of the halogen substituent may be expected to influence the monolayer structural parameters, particularly the nearest neighbor distance. Indeed, the lamella-backbone angle (ϕ) decreases with increasing substituent size, and the large iodine substituent is associated with the largest nearest neighbor distance (*c*).

Although the STM topographs shown in Figs. 1 *b–d* and 2 *b–d* are typical for the respective adsorbate species, the imaging of 1-fluorohexane monolayers met with significant difficulties, suggesting that, frequently, no ordered monolayer structure may exist. Even when imaged successfully, 1-fluorohexane monolayers exhibit a higher degree of disorder than those of other 1-halohexanes. An example of this effect is shown in Fig. 7*a*, where the spacing between adjacent adsorbate lamellae oscillates in a manner reminiscent of a zipper. Based on the adsorbate model shown in Fig. 2*a*, the uneven spacing seen in STM images may be due to frequent (head-to-tail) reversals of molecular orientation within a lamella. In contrast, individual domains extending over microns with few structural defects were observed for all other halohexanes, as exemplified by the 150 × 150-nm STM image of 1-iodohexane shown in Fig. 7*b*.

STM Image Contrast: Electronic and Spatial Factors. The arrays of overlaid molecules displayed in Fig. 2 and the structural parameters summarized in Table 1 imply very similar monolayer structures for all four 1-halohexanes. Thus, the pronounced differences in image contrast are likely primarily electronic in origin, arising from differences in shape and/or energy of the haloalkane electronic wave functions and their interaction with the graphite surface. In Figs. 1 and 2, the relative contrast of the halogen substituent is seen to increase successively from dark (i.e., darker than the hydrocarbon tail) in the case of fluorine to overwhelmingly bright in the case of iodine. An enhanced electron-tunneling rate for heavier halogen substituents is expected, given their lower ionization potential and the larger spatial extent of the heavier halogen substituent. A low

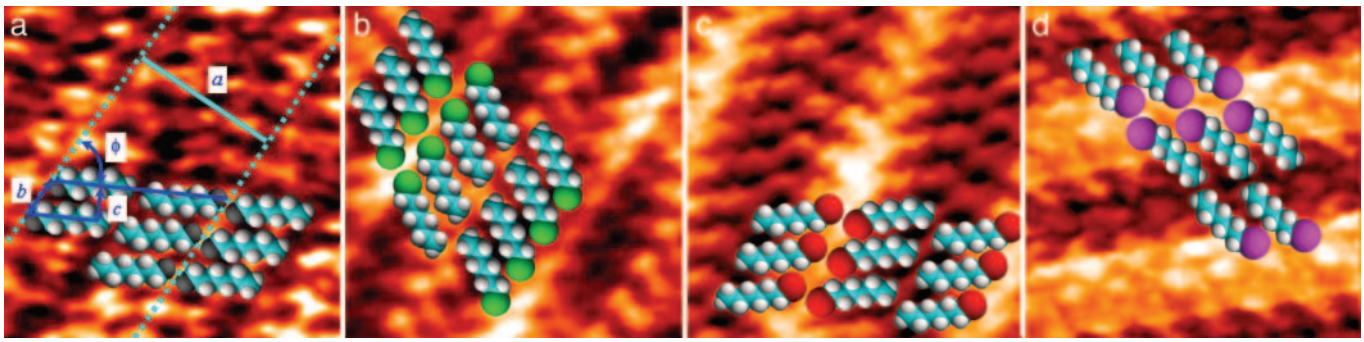

Fig. 2. High-resolution STM topographs of 1-halohexanes on HOPG. High-resolution (4 × 4 nm) constant current STM topographs are shown for 1-fluorohexane (V_{bias} = 2.0 V, I_{setp} = 100 pA) (*a*), 1-chlorohexane (V_{bias} = 1.9 V, I_{setp} = 90 pA) (*b*), 1-bromohexane (V_{bias} = 2.0 V, I_{setp} = 100 pA) (*c*), and 1-iodohexane (V_{bias} = 1.9 V, I_{setp} = 85 pA) (*d*). To minimize distortion in these small-scale images acquired at relatively slow absolute scan speeds (≈40 nm/s), a correction was applied for constant drift in the image plane, based on a careful analysis of measured adsorbate structural parameters as a function of absolute scan speed. Arrays of overlaid molecular models illustrate the proposed monolayer packing structure. The monolayer structural parameters (i.e., lamella spacing, *a*; neighbor spacing measured along the lamella direction, *b*; neighbor spacing measured perpendicular to the molecular backbone, *c*; and lamella-backbone angle, ϕ) highlighted in *a* are found to be similar for all 1-halohexanes (see Table 1), suggesting that the differences in image contrast are primarily electronic in nature. The dotted and solid light blue lines in *a* correspond to those shown in Fig. 1.

Table 1. Structural parameters of 1-halohexane monolayers from STM images at $T_{substrate}$ = 80 K

Molecule	*a*,* nm	*b*,* nm	*c*,† nm	ϕ,†°
1-fluorohexane	1.8 ± 0.2	0.50 ± 0.05	0.45 ± 0.06	63 ± 4
1-chlorohexane	2.1 ± 0.1	0.50 ± 0.02	0.44 ± 0.03	61 ± 3
1-bromohexane	2.0 ± 0.1	0.53 ± 0.02	0.44 ± 0.03	57 ± 3
1-iodohexane	1.9 ± 0.1	0.63 ± 0.03	0.52 ± 0.05	56 ± 3

Structural parameters as defined in Fig. 2*a* are as follows: *a*, lamella spacing; *b*, neighbor distance measured along the lamella axis; *c*, the neighbor spacing measured perpendicular to the molecular backbone; and ϕ, the lamella–backbone angle. Values are ± SD.

*Structural parameters directly determined by means of the STM spot pattern.

†Structural parameters based on the proposed monolayer structure indicated by the overlaid molecular arrays in Fig. 2.

ionization potential places filled and empty molecular adsorbate states closer to the Fermi level, thereby providing enhancement of the tunneling process. Although a direct comparison of different alkyl derivatives is generally complicated by the presence of both electronic and geometric factors, the image contrast observed in the present work is in agreement with previous observations of bright bromine and iodine substituents (17, 41, 61) and dark fluorine substituents observed at liquid–solid interfaces (17, 62).

The image contrast of the 1-fluorohexane monolayer may be somewhat affected by the higher degree of disorder, whereas the contrast for 1-bromohexane and 1-iodohexane is dominated by the bright halogen substituent. The STM images of 1-chlorohexane, which is the intermediate halogen case, are shown in Figs. 1*b*, 2*b*, and 3 and reveal a highly ordered monolayer with a moderately bright halogen substituent. Fig. 3 shows STM images of the 1-chlorohexane monolayer as a function of bias voltage polarity and magnitude, respectively. To exclude imaging artifacts, the bias polarity was switched back and forth within a single image frame. As shown in Fig. 3*a*, the same contrast is recovered when switching back to the original polarity. When the bias voltage magnitude is changed (see Fig. 3*b*), subsequent frames also showed the recovery of the original image contrast. As shown in Fig. 3, the STM image contrast depends strongly on the magnitude as well as polarity of the bias voltage.

The local density of states is subject to substantially different contributions from states localized on the halogen, alkyl, and substrate moieties as a function of energy. One might also expect the chlorine substituent to serve as an "STM chromophore" for the chlorohexane and therefore contribute substantially to the bias dependent image contrast. Indeed, careful inspection of Fig. 3 reveals that the chlorine substituent exhibits consistently high brightness, relatively independent of bias voltage. Assuming the usual straight lamella structure (i.e., not undulating like the wavy line also visible in Fig. 3) and a distinct chlorine image contrast, the position of the chlorine substituent is most easily assigned to the thin straight lines (as exemplified by the left black arrow in Fig. 3*a* and the only black arrow in Fig. 3*b*) visible at positive sample polarity in Fig. 3. With the assumption of no sudden drift in the image plane upon bias change and extrapolating to the remaining parts of Fig. 3, the location of the chlorine substituent is found to exhibit consistently high brightness, relatively independent of the bias voltage. In contrast, the longer range, undulating pattern also visible in all 1-chlorohexane images is found to change appearance strongly upon bias change.

Assignment of the undulating intensity pattern to a moiré effect is in agreement with the incommensurate nearest-neighbor distances characteristic of the proposed monolayer structure (see *Overview of STM Images and the Spatial Structure of the Adsorbate Monolayers*; see also Fig. 2*b* and Table 1). The STM images displayed in Figs. 1*b*, 2*b*, and 3 consistently reveal moiré patterns with a period of approximately seven molecules within each lamella.

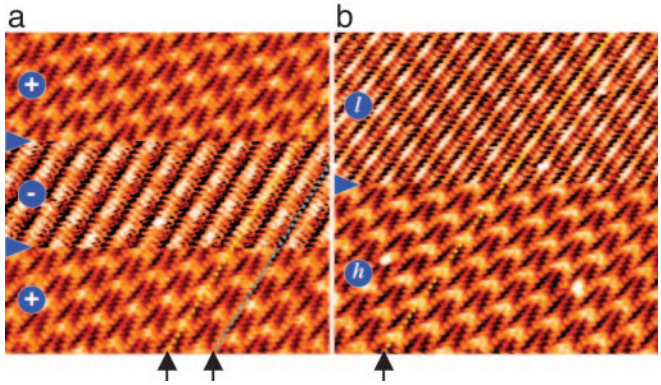

Fig. 3. Variation of bias voltage in STM topographs of 1-chlorohexane on HOPG. Constant-current STM topographs (25 × 25 nm) are shown for 1-chlorohexane where the bias voltage polarity (*a*) and magnitude (*b*) are varied. The lines where bias changes took place are marked by blue triangles. For each section of *a* ($|V_{bias}|$ = 2.0 V, I_{setp} = 90 pA), the choice of bias polarity is indicated by a blue + or −. Positive sample polarity leads to the appearance of thin bright stripes (e.g., starting at the left black arrow and following the yellow dashed line) due to the chlorine substituent, as well as broader, undulating bright stripes (e.g., starting at the right black arrow and following the blue dashed line), caused by a moiré effect. As emphasized by the yellow line, the location of the thin bright stripe at positive sample polarity (i.e., assigned as the position of the chlorine substituent) coincides with an intensity maximum at negative sample polarity. The high (V_{bias} = 2.1 V, I_{setp} = 100 pA) and low (V_{bias} = 1.75 V, I_{setp} = 100 pA) bias voltage sections in *b* are indicated by blue labels *h* and *l*. Although the features assigned to the chlorine substituent (e.g., starting at the black arrow and following the yellow dashed line) are consistently bright, the moiré effect depends strongly on the bias voltage magnitude.

In principle, the proposed monolayer structural parameters can be tested for consistency, given the known periodicity of the graphite substrate and the period of the moiré pattern. The repeat pattern of seven molecules suggests a nearest neighbor distance of 4.26 Å × 8/7 = 4.87 Å, which is in reasonable agreement with direct measurements (see distance parameter *c* in Table 1). However, closer inspection of Figs. 1*b*, 2*b*, and 3 reveals that the moiré pattern does not merely consist of an overall change in brightness from one molecule to the next within the same lamella. Rather, each molecular backbone exhibits an intensity variation, and the position of the maximum oscillates with a period of approximately seven molecules when moving along a lamella. This more complex moiré pattern is in qualitative agreement with the proposed angled monolayer structure, where the registry with the substrate not only shifts perpendicular to the molecular backbone (due to the "large" neighbor separation forced by the flat backbone plane) but also along the molecular backbone (due to the angled structure, i.e., $\phi \neq 90°$). Thus, the periodicity of seven molecules is likely to reflect in part the lateral shifts in registry (i.e., along the backbone), rather than only shifts perpendicular to the molecular backbone. This analysis is based on the assumption that the molecular axis is aligned with a high-symmetry direction of the underlying graphite substrate. Given the definite lack of commensurability, perfect substrate alignment may not be a good assumption for the short alkyl derivatives, which are the subject of the present study. Additional data are needed (e.g., STM images showing both an adsorbate domain and the graphite substrate) to unambiguously determine the relative orientation of molecular layer and underlying substrate. With that information, moiré patterns can be used for the quantitative validation of distance measurements (4).

Results from Theoretical Simulations: Driving Forces for Self-Assembly. Although a physisorbed self-assembled monolayer on a nonreactive surface in UHV at low temperature represents a fairly idealized model system from an experimental point of view, the

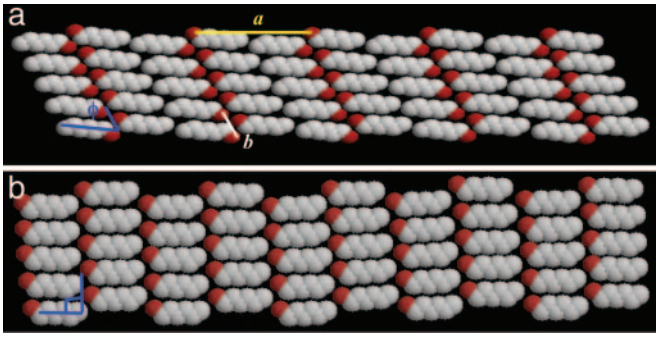

Fig. 4. Structures of a 1-bromohexane monolayer resulting from energy minimization. Adsorbate islands composed of 50 molecules are shown in two final calculated structures resulting from energy minimizations without periodic boundary conditions. Using the experimental monolayer structure as an initial guess for the energy minimization led to the angled head-to-head structure shown in *a*, whereas the rectangular head-to-tail structure shown in *b* resulted from using an intuitive head-to-tail arrangement as a starting point. The structural parameters *a*, lamella spacing; *b*, nearest-neighbor spacing; and ϕ, the lamella backbone angle, shown in *a*, are summarized in Table 2 for the calculated and experimental monolayers.

numerous interactions and degrees of freedom can still pose a challenge to theory. Because the search for the global minimum on the potential energy surface is hampered by a multitude of close-lying local minima, an educated guess about initial configurations is essential as a starting point for theoretical calculations. One approach taken in the present study is the use of the experimentally determined monolayer structure as an initial configuration for energy minimization.

The simulations were performed without the use of any periodic boundary conditions, and the resulting minimized structure of an adsorbate island composed of 50 1-bromohexane molecules is shown in Fig. 4*a*. The head-to-head structure of the initial configuration [with a molecular backbone/headgroup axis angle close to 60° (ϕ)] is retained. MD simulations (also performed without an imposed boundary condition) revealed this structure to be stable even up to 150 K (see Fig. 8), which is well above the experimental imaging temperature ($T_{\text{substrate}} = 80$ K).

To probe the energetics of the observed monolayer structure further, an alternative, more "intuitive" initial structure was constructed, based on the following considerations. Given the overall molecular dipole moment imposed by the terminal halogen substituent, the appearance of a head-to-tail motif might be expected, such that the bromine end in one lamella is closest to the CH_3 end of the molecules in the neighboring lamella. Fig. 4*b* illustrates the result of subjecting such an initial rectangular configuration (with reasonable nearest-neighbor distances in the range of 4.2–4.8 Å) (4, 5) to an energy-minimization procedure. The rectangular head-to-tail structure is maintained, with a molecular backbone/headgroup axis angle close to 90° (ϕ) and none of the offsets between adjacent molecules as seen for the head-to-head minimized structure. Molecular dynamics simulations performed on the head-to-tail structure showed high thermal stability beyond the experimental imaging temperature and no tendency toward disordering or angling.

Initial structures based on other experimental observations also were simulated. STM images recorded under ambient conditions showed that long 1-bromoalkanes formed self-assembled monolayers at the liquid/solid interface, where adjacent lamellae are in a head-to-head configuration (as they are in the UHV STM images of the present work) but with a rectangular structure, $\phi = 90°$ (unlike the UHV data where $\phi \cong 60°$) (17, 41, 61). Energy minimizations based on this initial configuration were found to lead inevitably to the angled structure shown in Fig. 4*a*. A comparison of the minimized monolayer structures shown in Fig. 4 with the proposed structures based on STM images (see Fig. 2) shows that the angled head-to-head structure of Fig. 4*a* is in agreement with the experimental structure, whereas the rectangular head-to-tail structure of Fig. 4*b* cannot be reconciled with the experimental data. In Table 2, the structural parameters associated with the minimized 1-bromohexane island shown in Fig. 4*a* are compared directly with experimental results. The agreement is found to be excellent. As shown in Table 3, the angled head-to-head structure is also preferable from a theoretical point of view, because it is associated with a lower total potential energy than the configuration of Fig. 4*b*.

Table 2. Structural parameters of 1-bromohexane monolayers: Experiment vs. theory

	a, nm	*b*, nm	ϕ, °
Experiment (UHV STM images)*	2.0 ± 0.1	0.53 ± 0.02	57 ± 3
Theory (energy minimization)†	1.99	0.55	58

The structural parameters *a*, *b*, and ϕ are defined in Table 1 and Fig. 2*a*.
*Structural parameters extracted from UHV-STM images (Figs. 1 and 2) acquired at $T_{\text{substrate}} = 80$ K. Values are ±SD.
†Theoretically predicted parameters extracted from the energy minimization of an adsorbate island composed of 50 molecules (Fig. 4*a*).

Given the successful reproduction of the experimental 1-bromohexane monolayer structure, the theoretical treatment provides a powerful tool with which to dissect the relevant interactions and uncover important driving forces for the formation of these self-assembled arrays. Not surprisingly, Table 3 shows that the substrate–adsorbate dispersion interactions represented through the Steele formulation are associated with the largest total contribution to the potential energy, making this component of the total monolayer energy the major driving force for the adsorption process.

The intermolecular interactions are dominated by LJ dispersion forces between alkyl chains that drive the close packing of adsorbed molecules, as well as by the slightly more favorable dispersive interactions of the polarizable bromine headgroups, which lie in close proximity for the head-to-head configuration. Even for the short 1-bromohexane species, Van der Waals interactions involving the entire molecule represent the largest numerical contribution to the molecule–molecule interaction energy.

The electrostatic forces and interactions of the functional groups (i.e., intermolecular dipole forces and image charge interactions with the surface) only account for a small fraction of the total energy. However, comparison of the two minimized structures in

Table 3. Interaction energies for the optimized self-assembly structures of two 1-bromohexane adsorbate islands on graphite

Energy	Angled head-to-head*	Rectangular head-to-tail†
Total potential energy	−1,081.99	−1,060.36
Stretch‡	0.02912	0.03219
Bend‡	0.20975	0.37962
Torsion‡	0.65999	0.58642
Electrostatic‡	−30.0781	−8.0681
LJ‡	−197.351	−191.479
Steele‡	−852.026	−852.333
Image charge‡	−3.42960	−9.47738

Values are in kilocalories per mole. Periodic boundary conditions were not employed in the energy minimizations.
*The energy-minimized, angled head-to-head structure for 50 1-bromohexane molecules on graphite is shown in Fig. 4*a*.
†The energy-minimized, rectangular head-to-tail structure for 50 1-bromohexane molecules on graphite is shown in Fig. 4*b*.
‡Individual contributions to the total potential energy are described in the text.

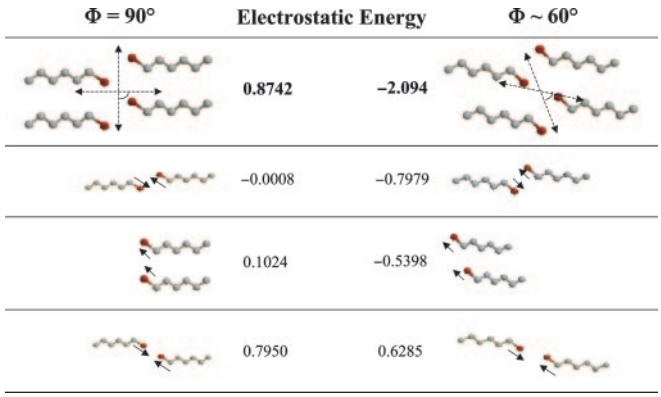

Fig. 5. Electrostatic interaction energies in angled vs. rectangular monolayer structures. An island of four 1-bromohexane molecules is displayed in a rectangular (i.e., lamella–backbone angle $\phi = 90°$; left side) and angled ($\phi \neq 90°$; right side) head-to-head configuration. The interaction energies shown (in kilocalories per mole) result from the partial charges in the OPLS force field assigned to the bromine substituents. Total electrostatic energies are given in the top row, whereas lower rows display the contribution of each nearest-neighbor electrostatic interaction.

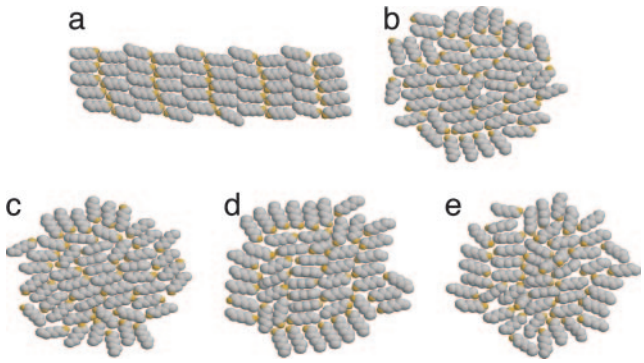

Fig. 6. Fifty 1-fluorohexane molecules after 50 ps of constant NVT molecular dynamics, followed by minimization. Starting from a minimized head-to-head structure, 50 molecule clusters of 1-fluorohexane were subjected to 50 ps of constant NVT molecular dynamics, followed by minimization in SIM. Structures were obtained at 0 K (the minimized head-to-head structure) (*a*), 50 K (*b*), 75 K (*c*), 100 K (*d*), and 150 K (*e*). A preference for head-to-tail pairing is seen in the center of each cluster beginning at 50 K. As the temperature is increased, the molecules become more densely packed and begin to angle out of the graphite plane.

Table 3 also reveals that the strong Steele and LJ interactions are relatively insensitive to the lamella–backbone angle and to the mutual orientation of headgroups (i.e., head-to-head vs. head-to-tail) so long as a close-packed monolayer structure is maintained. Table 3 shows that the ≈0.5 kcal/mol energetic advantage (measured per molecule) of the angled head-to-head structure can be ascribed almost completely to intermolecular electrostatic (i.e., dipole–dipole) forces. Thus, because of the sensitive angular dependence and subtle directional features of the carbon–halogen bond dipole (see discussion below in conjunction with Fig. 5), the relatively small electrostatic headgroup forces play a crucial role in driving the formation of the observed, angled head-to-head self-assembly.

To test the viability of analyzing a relatively small cluster of polar molecules and extrapolating electrostatic features (which are, of course, long-range) to a system the size of a complete monolayer, the energetics of the above two systems were recalculated as unit cells in a 2D infinitely replicated periodic system. The trends remained the same. Even in the infinite system described above, the angled molecular configuration was more energetically favorable.

A head-to-head configuration, where molecules in neighboring lamellae point their bromine substituents at each other, might appear "counterintuitive" considering the dipole–dipole interactions. Nevertheless, Table 3 identifies exactly this interaction as the crucial driving force favoring the head-to-head arrangement. As illustrated on the left side of Fig. 5, a head-to-head monolayer structure does indeed lead to the predicted unfavorable electrostatic interactions, when a rectangular lamella-backbone angle is maintained. For this molecular arrangement, two of three nearest-neighbor interactions are energetically approximately neutral, whereas one is unfavorable as expected (illustrated in the bottom row of Fig. 5). The energetically neutral interactions include one between neighboring molecules within the same lamella (see penultimate row in Fig. 5). This same interaction also occurs in the rectangular head-to-tail structure (see Fig. 4*b*). In such a head-to-tail configuration, the halogen substituents associated with adjacent lamellae are separated by one full molecular length, giving rise to little additional electrostatic interaction. As a result, the overall electrostatic energy associated with the rectangular head-to-tail structure is smaller in magnitude, as can be seen in the right column of Table 3. In contrast, the angled head-to-head structure is associated with two (of three) favorable nearest neighbor electrostatic interactions, as can be seen on the right side of Fig. 5, leading to an overall very favorable electrostatic energy. Essentially, the localization of the molecular dipole on the terminal C–Br bond, the oblique lamella–backbone angle, and the offset of molecular rows in adjacent lamellae conspire to create nearly optimal electrostatic attractive forces. These features allow headgroup interactions to play an important role in driving the self-assembly, even in the presence of overwhelmingly strong alkyl chain interactions.

To put the strength of this interaction into perspective, it is useful to compare this system with one with classical hydrogen bonds. The head-to-tail configuration shown in Fig. 4*b* would most closely represent the juxtaposition of an electron-rich endgroup with hydrogen atoms. However, the methyl groups are not polar in these haloalkanes, and so there is no strong attraction that resembles a hydrogen-bond-like force, which consists mainly of a very strong electrostatic component with some additional Van der Waals interactions. In quantitative terms, the electrostatic interaction between the Br headgroups in the head-to-head configuration is also much smaller than a typical hydrogen bond, which makes its influence on the self-assembly all the more remarkable.

The fascinating subtleties of intermolecular headgroup driving forces uncovered in the analysis of the 1-bromohexanes on graphite open up the question of the behavior of the corresponding fluorinated molecules in a UHV-STM experiment. Does the smaller and more electronegative F headgroup exhibit different packing properties than do the large, polarizable Cl, Br, I functionalities, even to the point of assembling in a head-to-tail manner?

Preliminary theoretical studies on the 1-fluorohexane systems, performed in a manner identical to that described previously for the brominated alkanes, do indeed show a very different structure and ordering pattern than the rest of the halohexane series. Upon minimization (Fig. 6*a*), this molecule also exhibits angling away from a head-to-head rectangular structure, but the energetic gain from adopting this type of offset arrangement is not nearly as drastic as in the bromohexane case. Furthermore, this configuration is completely unstable at higher temperatures, as shown in Fig. 6 *b–e*, which includes four configurations of 50 molecule clusters after constant NVT dynamics at 50, 75, 100, and 150 K. In each case, the final structure observed after 50 ps of molecular dynamics at the indicated temperature then was energy minimized. This procedure allows the direct comparison, both numerically and visually, of the configurations resulting from each dynamics simulation, at an effective temperature of 0 K. The energetic breakdown for each of the structures in Fig. 6 is given in Table 4. After adding even the

Table 4. Energetics for the structures shown in Fig. 6 for 1-fluorohexane molecules after molecular dynamics at the indicated temperature followed by minimization

Temperature, K	Total potential energy	Electrostatic*	LJ*	Steele*	Image charge*
50	−1,716.416	1,091.970	−142.4635	−687.0708	−2,010.433
75	−1,731.039	1,129.290	−142.7915	−674.8799	−2,068.707
100	−1,725.193	1,178.190	−151.9625	−656.7464	−2,128.838
150	−1,625.716	1,238.707	−153.8704	−601.3439	−2,217.655

Values are in kilocalories per mole.
*Individual contributions to the total potential energy are described in the text.

relatively small amounts of energy associated with a 50 K simulation, the monolayer completely reordered, while in all cases maintaining a close-packed structure. In fact, as the temperature is increased, the molecules tend to pack ever more tightly. This effect is the opposite of what might have been expected in an unbounded, higher temperature simulation, where the free exploration of the graphite surface would give a large entropic advantage to arrangements where molecules drift apart. The energetic (enthalpic) advantage of this rearrangement dominates the entropic factors.

A detailed analysis of the energetics of the 50, 75, and 100 K structures (Table 4) shows that despite the obvious differences in observable structure, the three configurations are almost identical in total potential energy. There is a clear edge effect in each case, and the internal portions of the domains seem to be arranged almost haphazardly. As the temperature is increased, the electrostatic interactions (from both real and image charges) drive the structure toward a configuration where the alkyl backbone begins to angle out of the plane of the surface, resulting in the more closely packed structures seen at 75 and 100 K. The higher energy states accessible at 150 K and above (data not shown) allow a further desorption of the entire backbone to occur so that the fluorine substituents can begin to point into the surface, lying in closer proximity to their image charges.

In contrast to the 1-bromohexane case, the LJ energies for 1-fluorohexane are not the largest intermolecular energetic term; however, in both structures the subtleties of the electrostatic interactions drive the formation of the monolayer structure The theoretical data indicates that the fluorinated system does not differentiate to any great extent between the head-to-head vs. head-to-tail dimer conformations. The much greater disorder observed experimentally in the 1-fluorohexane images as compared with the other halohexanes may have its origins in this effect. Because of the drastic edge effects observed in the 1-fluorohexane simulations, much larger clusters must be studied in the future to ascertain that the internal section structure of the system is representative of that formed experimentally and is theoretically sound with respect to size artifacts.

To further test the importance and influence of image charges in the potential, the same dynamic simulations were run again on the 50-molecule minimized 1-fluorohexane cluster with the image potential removed from the energy expression. The molecules in this simulation did not maintain any long-range structure at all (see Fig. 9). Instead, the monolayer separated into two- to four-molecule groupings, driven apart by the very repulsive electrostatic energy, while still maintaining some of the favorable short-range Van der Waals attraction within the small clusters.

The compact, electronegative fluorine substituent gives rise to electrostatic interactions of a magnitude comparable to the dispersion interactions associated with the alkyl chain. Consequently, the role of the fluorine headgroup may not be limited to simply driving the lamella–backbone angle; instead, the minimization of the overall energy may entail the disruption of the usually dominant alkyl–alkyl or alkyl–surface interactions.

In principle, partial detachment of alkyl chains from the surface can occur because of the electrostatic interactions and may provide several benefits. First, reducing the footprint of each molecule allows for a larger number of headgroup–surface interactions per unit area and for stronger intermolecular electrostatic forces, because the partially charged endgroups can lie in much closer proximity to each other in this configuration than in a flat conformation. Second, because of their anisotropy, headgroup forces may benefit from the additional degrees of freedom available in partially detached molecules. This trend is consistent with the relative difficulty in recording UHV STM images of ordered 1-fluorohexane monolayers, in contrast to the predictable long-range order seen in the STM images of the rest of the halohexane series in UHV.

Further theoretical calculations using different conditions and higher temperatures (data not shown) suggest the existence of an additional, denser adsorbate phase, analogous to the crystalline phases exhibited by alkane thiol monolayers on Au(111) (29). During monolayer growth, some alkane thiols undergo a phase transition from a "flat" low-density structure (similar to the "typical" structure of alkane derivatives on graphite) to the well known higher-density structure where only the headgroups are in direct contact with the surface (29). In contrast, monolayers of nonfunctionalized alkanes on gold only exhibit the flat, low-density structure (27, 30). The strong headgroup–surface interaction characteristic of the thiol-on-gold system is crucial for the formation of the high-density phase. Correspondingly, the electrostatic headgroup–surface interactions of the 1-fluorohexane-on-graphite system may be nearly sufficient to drive a phase transition to a higher density monolayer structure. Future experimental studies using variable temperature-annealing procedures that examine 1-fluoroalkane self-assembly as a function of alkyl chain length and coverage are needed.

The above analysis of the driving forces leading to partially disordered 1-fluorohexane monolayers highlights the delicate balance of interactions required for the formation of a well defined adsorbate structure. For the other 1-halohexanes, the balance of forces between the electrostatic headgroup interaction and the alkyl, interchain Van der Waals interactions is less obvious. A comparison of potential energies for two visually distinct minimized monolayer structures of 1-bromohexane (see Table 3) does not reveal any significant energy penalty for the intermolecular Van der Waals (dispersion) interactions as a result of optimizing the electrostatic headgroup interactions through lamella–backbone angling.

Neverthless, all of the 1-bromohexane monolayer structures resulting from energy minimization share an additional feature regarding molecular orientation. The backbone plane of 1-bromohexane molecules is always found to be oriented parallel to the surface plane (a flat configuration), in contrast to nonfunctionalized alkanes on graphite, where experimental data indicate a variable backbone orientation (4, 5, 7, 42–44). As discussed above, the orientation of the molecular backbone plane affects the nearest-neighbor distance of the adsorbate layer (4, 7) and therefore influences the tradeoff between molecule–graphite and molecule–molecule dispersion interactions (47). Thus, the unique electrostatic and geometric properties associated with the large size of the polarizable bromoalkane headgroup affect the balance of dispersion interactions by pinning the molecular backbone plane parallel to the surface plane. This finding is in stark contrast to the

fluorohexane molecules, which, because of their small, electronegative headgroup, have a much larger relative electrostatic contribution as compared with the Van der Waals forces on the adjacent atoms, and so they are driven to maximize the electrostatics through backbone desorption, which allows the closest proximity of the real and image charges, even at the expense of adsorption energy. The energetic signature of such competing constraints has been revealed in our previous experimental examination of thermal desorption spectra as a function of alkane functionalization and chain length (47).

Through a subtle balancing of both the angle between the lamella and backbone axes and the angle between the surface and backbone planes, headgroup interactions in functionalized alkanes on graphite enter into competition with alkyl chain dispersion forces. The present study has shown that a completely ordered and regular angled head-to-head structure results for the 1-chlorohexane, 1-bromohexane, and 1-iodohexane monolayers on graphite under UHV conditions, and a more disordered but tightly packed structure is observed for 1-fluorohexane. In contrast, nearly rectangular structures have been observed in ambient STM images of 1-bromoalkane monolayers at the liquid/solid interface (i.e., in the presence of solvent) (17, 41, 61). Further studies are needed to elucidate the ability of solvent to shift the monolayer structure by tilting the balance among these interactions.

Summary and Conclusions

The self-assembly of 1-halohexanes on graphite has been studied in a concerted experimental and theoretical effort. UHV STM images acquired at $T_{\text{substrate}} = 80$ K reveal an essentially identical, angled head-to-head configuration for all 1-halohexane monolayers, with differences in image contrast ascribed to electronic factors. The lack of commensurability following from the monolayer structural parameters is qualitatively consistent with the observed moiré patterns in the STM images.

For 1-bromohexane, the results from energy minimizations and molecular dynamics simulations are in quantitative agreement with the experimentally determined monolayer structures. Thus validated, the theoretical studies permit an analysis of the competing interactions driving the self-assembly. Electrostatic headgroup interactions are found to be small in magnitude yet play an important role because of their anisotropy. While alkyl chain dispersion interactions drive the formation of a close-packed monolayer composed of all-trans extended molecules, headgroup forces compete successfully to control both the angles between the lamella and backbone axes and between the surface and backbone planes.

Consistent with this concept of competing interactions, adsorption energies measured as a function of alkyl chain length and functionalization reveal the presence of energetic tradeoffs (47). In the case of 1-fluorohexane, the calculations indicate that the presence of significant electrostatic headgroup forces leads to the disruption of alkyl chain dispersion interactions and, therefore, results in a large number of energetically similar structures. Accordingly, STM images of 1-fluorohexane monolayers exhibit a greater degree of disorder than observed for any of the other 1-halohexanes.

By focusing on the self-assembly of simple model systems in UHV (i.e., in the absence of solvent), the present study has revealed a particularly appealing consistency between experiment and theory. The balance of interactions determining the self-assembled structures has been dissected in detail. Further studies are needed to build on these results by reexamining self-assembly in the presence of solvent.

We thank Dr. John Polanyi for a number of insightful suggestions, Dr. William L. Jorgensen for force-field and parameter-fitting assistance, and Dr. Harry Stern for many helpful discussions and the use of SIM. This work was supported by National Science Foundation Grants CHE-03-52582 and CHE-03-16896, National Science Foundation Materials Research Science and Engineering Centers Grant DMR-02-13574), and the New York State Office of Technology, Science, and Academic Research. G.M.F. was supported by the Dreyfus Foundation's environmental science postdoctoral training program.

1. Bien-Vogelsang, U. & Findenegg, G. H. (1986) *Colloids Surf.* **21,** 469–481.
2. McGonigal, G. C., Bernhardt, R. H. & Thomson, D. J. (1990) *Appl. Phys. Lett.* **57,** 28–30.
3. McGonigal, G. C., Bernhardt, R. H., Yeo, Y. H. & Thomson, D. J. (1991) *J. Vac. Sci. Techn. B* **9,** 1107–1110.
4. Rabe, J. P. & Buchholz, S. (1991) *Science* **253,** 424–427.
5. Liang, W., Whangbo, M. H., Wawkuschewski, A., J., C. H. & Magonov, S. N. (1993) *Adv. Mater.* **5,** 817–821.
6. Gunning, A. P., Kirby, A. R., Mallard, X. & Morris, V. J. (1994) *J. Chem. Soc. Faraday Trans.* **90,** 2551–2554.
7. Herwig, K. W., Matthies, B. & Taub, H. (1995) *Phys. Rev. Lett.* **75,** 3154–3157.
8. Couto, M. S., Liu, X. Y., Meekes, H. & Bennema, P. (1994) *J. Appl. Phys.* **75,** 627–629.
9. Elbel, N., Roth, W., Gunther, E. & Vonseggern, H. (1994) *Surf. Sci.* **303,** 424–432.
10. Venkataraman, B., Breen, J. J. & Flynn, G. W. (1995) *J. Phys. Chem.* **99,** 6608–6619.
11. Cyr, D. M., Venkataraman, B. & Flynn, G. W. (1996) *Chem. Mater.* **8,** 1600–1615.
12. Cyr, D. M., Venkataraman, B. & Flynn, G. W. (1996) *J. Phys. Chem.* **100,** 13747–13759.
13. Hibino, M., Sumi, A. & Hatta, I. (1996) *Thin Solid Films* **273,** 272–278.
14. Yeo, Y. H., McGonigal, G. C. & Thomson, D. J. (1993) *Langmuir* **9,** 649–651.
15. Fang, H., Giancarlo, L. C. & Flynn, G. W. (1999) *J. Phys. Chem. B* **103,** 5712–5715.
16. Giancarlo, L. C., Fang, H., Rubin, S. H., Bront, A. A. & Flynn, G. W. (1998) *J. Phys. Chem. B* **102,** 10255–10263.
17. Giancarlo, L. C. & Flynn, G. W. (1998) *Annu. Rev. Phys. Chem.* **49,** 297–336.
18. Yablon, D. G., Giancarlo, L. C. & Flynn, G. W. (2000) *J. Phys. Chem. B* **104,** 7627–7635.
19. Yablon, D. G., Jinsong, G., Knapp, D., Fang, H. & Flynn, G. W. (2001) *J. Phys. Chem. B* **105,** 4313–4316.
20. Kwon, S. J., Russel, J., Zhao, X., Vidic, R. D., Johnson, J. K. & Borguet, E. U. (2001) *Langmuir* **18,** 2595–2600.
21. Paserba, K. R. & Gellman, A. J. (2001) *Phys. Rev. Lett.* **86,** 4338–4341.
22. Paserba, K. R. & Gellman, A. J. (2001) *J. Chem. Phys.* **115,** 6737–6751.
23. Shukla, N., Gui, J. & Gellman, A. J. (2001) *Langmuir* **17,** 2395–2401.
24. Xu, Q.-M., Wan, L.-J., Wang, C. & Bai, C.-L. (2001) *Surf. Interface Anal.* **32,** 256–261.
25. Kwon, S. J., Vidic, R. D. & Borguet, E. U. (2002) *Carbon* **40,** 2351–2358.
26. Kwon, S. J., Vidic, R. D. & Borguet, E. U. (2002) *Surf. Sci.* **522,** 17–26.
27. He, Y., Ye, T. & Borguet, E. (2002) *J. Phys. Chem. B* **106,** 11264–11271.
28. Claypool, C. L., Faglioni, F., Goddard, W. A., III, Gray, H. B., Lewis, N. S. & Marcus, R. A. (1997) *J. Phys. Chem. B* **101,** 5978–5995.
29. Poirier, G. E. (1997) *Chem. Rev.* **97,** 1117–1127.
30. Xie, Z. X., Xu, X., Tang, J. & Mao, B. W. (2000) *J. Phys. Chem. B* **104,** 11719–11722.
31. Wintgens, D., Yablon, D. G. & Flynn, G. W. (2003) *J. Phys. Chem. B* **107,** 173–179.
32. Yablon, D. G., Wintgens, D. & Flynn, G. W. (2002) *J. Phys. Chem. B* **106,** 5470–5475.
33. Askadskaya, L. & Rabe, J. P. (1992) *Phys. Rev. Lett.* **69,** 1395–1398.
34. Bucher, J. P., Roeder, H. & Kern, K. (1993) *Surf. Sci.* **289,** 370–380.
35. Hibino, M. & Hatta, I. (1995) *Jpn. J. Appl. Phys.* **34,** 610–614.
36. Hibino, M., Sunni, A., Tsuchiya, H. & Hatta, I. (1998) *J. Phys. Chem. B* **102,** 4544–4547.
37. Schulze, J., Stevens, F. & Beebe, T. P., Jr. (1998) *J. Phys. Chem. B* **102,** 5298–5302.
38. Stevens, F., Patrick, D. L., Cee, V. J., Purcell, T. J. & Beebe, T. P., Jr. (1998) *Langmuir* **14,** 2396–2401.
39. Hansen, F. Y., Herwig, K. W., Matthies, B. & Taub, H. (1999) *Phys. Rev. Lett.* **83,** 2362–2365.
40. Stevens, F. & Beebe, T. P., Jr. (1999) *Langmuir* **15,** 6884–6889.
41. Giancarlo, L. C. & Flynn, G. W. (2000) *Acc. Chem. Res.* **33,** 491–501.
42. Hentschke, R., Schürmann, B. L. & Rabe, J. P. (1992) *J. Chem. Phys.* **96,** 6213–6221.
43. Krishnan, M., Balasubramanian, S. & Clarke, S. (2003) *J. Chem. Phys.* **118,** 5082–5086.
44. Krim, J., Suzanne, J., Shechter, H., Wang, R. & Taub, H. (1985) *Surf. Sci.* **162,** 446–451.
45. Morishige, K., Takami, Y. & Yokota, Y. (1993) *Phys. Rev. B* **48,** 8277–8281.
46. Fang, H., Giancarlo, L. C. & Flynn, G. W. (1998) *J. Phys. Chem.* **102,** 7311–7315.
47. Müller, T., Flynn, G. W., Mathauser, A. T. & Teplyakov, A. V. (2003) *Langmuir* **19,** 2812–2821.
48. Jorgensen, W. L. (1986) *J. Phys. Chem.* **90,** 1276.
49. Jorgensen, W. L. (1998) in *Encyclopedia of Computational Chemistry*, ed. Schleyer, P. V. R. (Wiley, New York), Vol. 5, pp. 3281–3285.
50. Dewar, M. J. S., Healy, E. F. & Stewart, J. J. P. (1985) *J. Am. Chem. Soc.* **107,** 3902.
51. Stewart, J. J. P. (1989) *J. Comp. Chem.* **10,** 209–220.
52. Steele, W. A. (1973) *Surf. Sci.* **36,** 317.
53. Hammonds, K. D., McDonald, I. R. & Tildesley, D. J. (1993) *Mol. Phys.* **78,** 173.
54. Lang, N. D. & Kohn, W. (1973) *Phys. Rev. B* **7,** 3541.
55. Velasco, E. & Peters, G. H. (1995) *J. Chem. Phys.* **102,** 1098.
56. Peters, G. H. & Velasco, E. (1995) *Mol. Physics* **84,** 1039.
57. Schlick, T. & Fogelson, A. (1992) *ACM Trans Math Software* **18,** 71–111.
58. Martyna, G. J., Klein, M. L. & Tuckerman, M. (1992) *J. Chem. Phys.* **97,** 2635–2643.
59. Nose, S. (1984) *J. Chem. Phys.* **81,** 511–519.
60. Small, D. M. (1986) *The Physical Chemistry of Lipids: From Alkanes to Phospholipids* (Plenum, New York).
61. Giancarlo, L. C., Cyr, D. M., Muyskens, K. & Flynn, G. W. (1998) *Langmuir* **14,** 1465–1471.
62. Stabel, A., Dasaradhi, L., O'Hagan, D. & Rabe, J. P. (1995) *Langmuir* **11,** 1427–1430.